REVISTA MEXICANA DE FÍSICA S **57** (1) 21–29 FEBRERO 2011

Synchrotron radiation study of the uranium chemical species electrodeposited for alpha spectrometry sources

D.C. Burciaga-Valencia[a], C.G. Méndez[a], H. Esparza-Ponce[a], A.M. Beesley[b], M.T. Crespo[c], L. Fuentes-Cobas[a], L. Fuentes-Montero[a,d], and M.E. Montero-Cabrera[a]*

[a]*Centro de Investigación en Materiales Avanzados, S.C., Miguel de Cervantes 120, Complejo Ind. Chihuahua, Chihuahua, Chih., México.*

*e-mail: elena.montero@cimav.edu.mx

[b]*School of Chemical Engineering and Analytical Science, The University of Manchester, United Kingdom.*

[c]*Laboratorio de Metrología de Radiaciones Ionizantes, Centro de Investigaciones Energéticas, Medioambientales y Tecnológicas, Madrid, Spain.*

[d] *Now in: Institute Laue Langevin, Grenoble, France.*

Recibido el 10 de marzo de 2010; aceptado el 31 de agosto de 2010

Alpha spectrometry (AS) with semiconductor detectors has applications in nuclear decay data measurements, environmental, geological and nuclear wastes studies and other works requiring determination of actinide and other alpha emitter contents. In order to obtain accurate measurements by producing good resolution alpha spectra, AS sources must be thin and uniform. AS sources produced by electrodeposition consist of a radioactive deposit onto a metallic substrate (cathode of the electrolytic cell). Natural U sources prepared by the Hallstadius method have co-deposited Pt, originated from the dissolution of the anode during the electrodeposition. A recent work published elsewhere has reported a study on the morphology and spatial distribution of the U/Pt deposits with the related chemical speciation of U, using scanning electron microscopy with energy dispersive X-Ray spectroscopy, X-Ray photoelectron spectroscopy and X-Ray absorption fine structure (XAFS).

The purpose of this work is to explain the structure of the Pt/U deposits. We have obtained new spectra of the U LIII edge XAFS by total electron yield at Stanford Synchrotron Radiation Lightsource (SSRL), BL 2-3. Grazing incidence X-Ray diffraction (GI-XRD) patterns were obtained at SSRL, BL 11-3. GI-XRD patterns show a bimodal distribution of grain sizes of Pt, with dimensions $\sim$ 5 and 20 nm; schoepite diffraction signals suggest grain dimensions of $\sim$5 nm, *i.e.* with low crystallization. XAFS spectra were fitted assuming two different structures: uranyl hydroxide and schoepite, and results were compared. U-U path shows low intensity that also may be a result of low crystallization.

Keywords: Uranium; gracing incidence X-Ray diffraction; X-Ray absorption fine structure; synchrotron radiation

La espectrometría alfa (EA) con detectores de semiconductor tiene aplicaciones en mediciones de datos para desintegraciones nucleares, estudios ambientales, geológicos y de residuos nucleares, así como en otros trabajos que requieran la determinación de contenidos de actínidos y otros emisores alfa. Para obtener buenas medidas, las fuentes para EA deben ser finas y de forma que permitan obtener espectros alfa con buena resolución energética. Las fuentes para EA producidas por electrodeposición consisten en un depósito radiactivo sobre un sustrato metálico (cátodo de la celda electroquímica). Las fuentes de U natural preparadas por el método de Hallstadius contienen Pt co-precipitado, originado por la disolución del ánodo durante la electrodeposición. Un trabajo recientemente publicado presenta un estudio sobre la morfología y distribución espacial de los depósitos de U/Pt en relación con la especiación química del U, usando microscopía electrónica de barrido con espectroscopía de rayos X dispersiva en energía, espectroscopía de fotoelectrones de rayos X y de estructura fina de la absorción de rayos X (XAFS).

El propósito del presente trabajo es explicar la estructura de los depósitos de Pt/U. Se han obtenido nuevos espectros del borde de absorción U LIII por salida total de electrones en el haz 2-3 de la Fuente de Radiación Sincrotrónica de Stanford (SSRL). Los patrones de difracción de rayos X de incidencia rasante (GI-XRD) muestran una distribución bimodal de tamaño de grano del Pt, con dimensiones de 5 a 20 nm; el patrón de difracción de la schoepita sugiere dimensiones de $\sim$5 nm, es decir, de baja cristalización. Los espectros de XAFS se ajustaron asumiendo dos estructuras diferentes: el hidróxido de uranilo y la schoepita, y los resultados se compararon. Las trayectorias fotoelectrónicas U-U muestran bajas intensidades, lo que también puede deberse a baja cristalización.

Descriptores: Uranio; difracción de rayos X con incidencia rasante; estructura fina de la absorción de rayos X; radiación sincrotrónica

PACS: 61.05 cj; 61.05 cp

1. Introduction

High resolution alpha spectrometry (AS) is commonly used in a large number of applications such as nuclear decay data measurements [1], environmental [2], geological [3], nuclear wastes characterization [4] and health studies [5]. To produce accurate measurements, it is generally assumed that thin and uniform sources have been prepared [6,7], being electrodeposition the most common technique of source preparation for routine measurements [8]. Alpha sources produced by electrodeposition consist of a radioactive deposit onto a metallic substrate (cathode of the electrolytic cell) [9]. It has been demonstrated the presence of co-deposited platinum in the deposit when a sulphate-containing electrolyte is used [10-13], originated from the dissolution of the anode

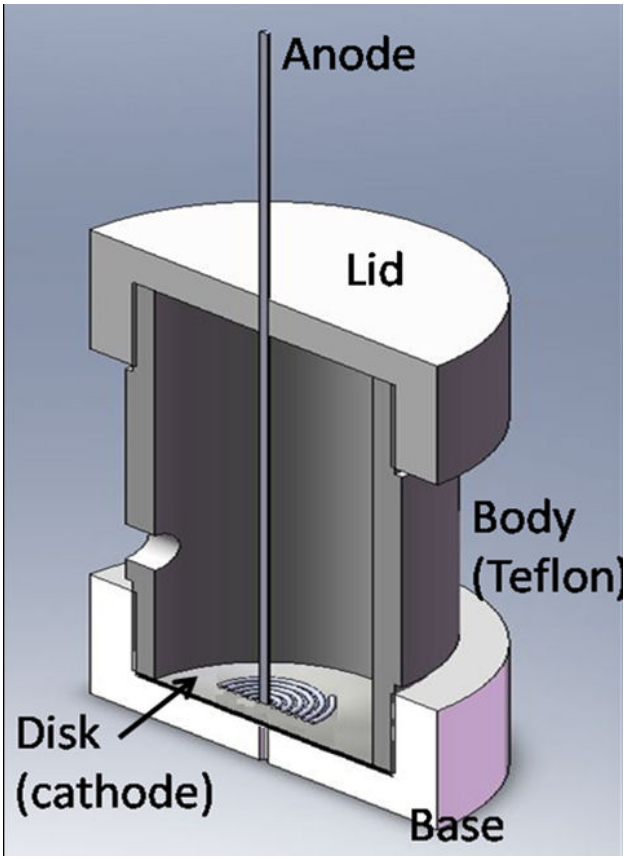

FIGURE 1. Transversal view of the electrolytic cell for deposition of uranium.

during the electrodeposition. This is an important fact since many of the most popular methods of electrode position [9,14,15] include sulphate ions as components of the aqueous electrolyte.

In a recent paper by Beesley *et al.* [13], the morphology and composition of natural uranium sources prepared by the Hallstadius method, with co-deposited platinum were studied by scanning electron microscopy/energy dispersive spectroscopy (SEM-EDX), X-ray photoelectron spectroscopy (XPS) and X-ray absorption fine structure (XAFS). However, no conclusive information concerning the phase identification of uranium deposits were presented. This factor is relevant not only for uranium sources, but also for sources of other long half-life radionuclides which contribute with significant mass to the deposits that can in turn affect the expected energy resolution of alpha spectra obtained from them.

The aim of the present work is to report results about identification of chemical species of Pt and U in the electrodeposition process obtained by synchrotron radiation grazing incidence X-ray diffraction (GI-XRD) and by new XAFS data.

2. Materials and methods

2.1. Sample preparation

All sources were prepared by the Hallstadius method [14] from a sulphuric acid electrolyte at pH 2.1-2.4, with Na_2SO_4 to prevent adsorption onto the walls of the electrodeposition cells. Deposition was carried out onto mirror polished stainless steel disks (2.5 cm diameter, 2.2 cm diameter of active area, 1 mm thickness) acting as cathode, while the anode was a 1 mm diameter platinum wire folded in the base into spiral shape of 15 mm diameter. Current densities of 0.52 A cm^{-2} and 7 mm distance between electrodes were used. Figure 1 shows schematic diagram of the electrolytic cell.

Two sets of sources were studied in this paper as summarized in Table I, where uranium content and studies performed over them are specified. Each set consists of three sources obtained at electrodeposition times of 20, 40 and 60 minutes, respectively. The first set was studied in Beesley *et al.* [16] (CIEMAT-Unat in Table I). These sources were prepared at CIEMAT from 0.6 mL of a CIEMAT natural uranium standard solution of 6.15 $\pm$ 0.15 Bq/g activity concentration in 1 M HNO_3. The other set of sources was prepared at CIMAV (CIMAV-UAc in Table I). It was prepared by adding 157 μL of a uranyl acetate solution of 13.65 $\pm$6 % Bq/mL (Polyscience Inc, containing depleted uranium, activity ratio U-234/U-238 = 0.156 $\pm$ 0.008 [22]) dissolved in acetic acid at pH 4 to the sulfuric electrolyte. All electrodeposition experiments for the same set of samples were performed with the same initial amount of uranium. In consequence, for CIEMAT-Unat, the electrodeposition yield is about 100% for the 60 minutes electrodeposition time sources and decreases to about 77% when the time decreases. For CIMAV-UAc set, the yield varies in the range 80-57%, being always the highest values for the 60 minutes electrodeposition times.

TABLE I. Set of prepared sources, included in the present study.

Sample	Uranium mass (μg)	Set	Studies performed over samples reported in the present work
U15-20	128	CIEMAT-Unat	XAFS (SSRL), AS (Manchester)
U5-40	131		
U14-60	153		
U12-20	128		
U4-30	120		
U13-40	134		
U17-60	155		
UAc-20	107	CIMAV-UAc	XAFS (SSRL), GI-XRD (SSRL)
UAc-40	85		
UAc-60	116		

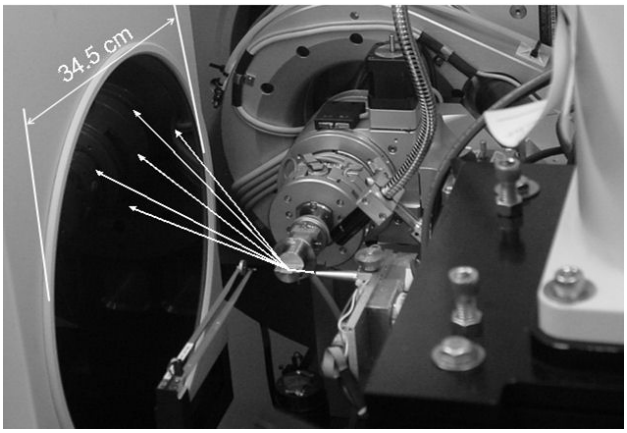

FIGURE 2. Experimental arrangement at the beamline 11-3, at SSRL: To the left, 2-D position sensitive GI-DRX detector; at center left, sample holder with a sample on it and to center right, XR collimator.

2.2. Experiments

AS on the sets of samples CIEMAT-Unat has been performed at Manchester, using a CANBERRA Model 7401 Alpha Spectrometer, with a 100 mm^2 PIPS®Detector. Counting distance of sample-detector was 25 mm. For each experiment a complete spectrum of 4096 channels was accumulated. In order to obtained information regarding resolution of the sources, the counting time was set to 36 h.

GI-XRD patterns were obtained at SSRL, at beamline 11-3. The experimental facility is described elsewhere [16,17]. The experimental setup and calibration conditions used in the detection were as follows: 2D-detector diameter = 345 mm; pixel size = 0.1 mm; X-ray spot size=0.1 mm 2D position-sensitive detector calibrated with a LaB_6 standard sample; sample detector distance=150 mm; incidence angle = $(0.5 \pm 0.5)°$; X-ray wavelength λ =0.97354 Å; Experimental 2D patterns processed by means of software Fit-2D [18]. Figure 2 shows the experimental arrangement at the beamline.

XAFS experiments at the UL_3-edge, performed on both sets, were carried out at the Stanford Synchrotron Radiation Lightsource (SSRL) beamline 2-3. The SPEAR-3 storage ring was operated at 3.0 GeV with a beam current of 100 mA. We used a Si(220) double crystal monochromator, $\varphi = 0$. The beam size was 1.0 mm x 10.0 mm. XAFS U L_3 spectra were acquired in total electron yield mode using the collector current. Data were recorded on an energy grid of 10 eV/step in the pre-edge region and 0.35 eV/step in the remaining X-ray Absorption Near Edge Spectra (XANES) region, with an integration time of 1 s/step. An energy calibration of the beam was performed by collecting the transmission spectra of a reference Y foil at the Y K edge. A total of 6 scans were obtained for each source. Spectra obtained from sources of the same electrodeposition time were averaged together. For calibration and alignment of XANES spectra the software Athena, the front-end for IFEFFIT, was employed [19].

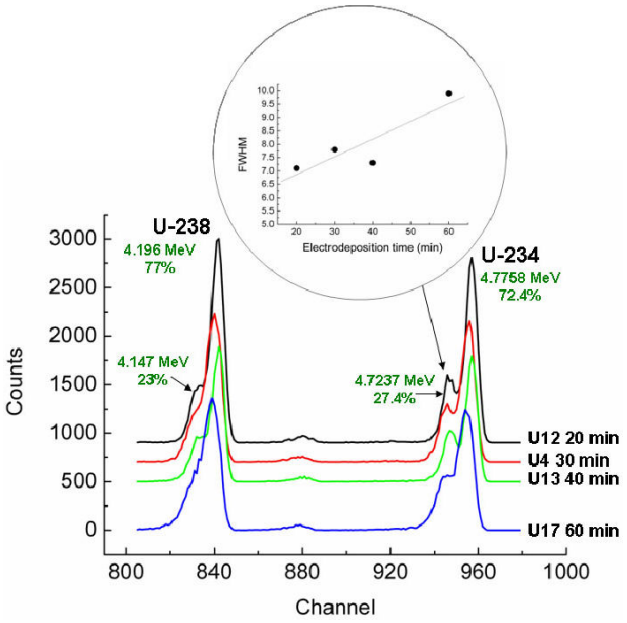

FIGURE 3. High resolution alpha spectra obtained from four samples of the CIEMAT Unat set. Spectra are vertically shifted for clarity.

EXAFS data were processed and analyzed using the Athena 0.8.061 and Artemis 0.8.014 graphical interfaces versions [19] to IFEFFIT [20]. Calibrated scans were averaged and background-substracted. Spline fitting was performed using the Autobk parameters R_{bck}=0.75, k-weight=3 and dk=1. The atomic coordinates from the published Schoepite XRD-derived crystal structure [21] and uranyl hydroxide [22] were used to generate 4.5 Å radius clusters for the calculations. Coordination numbers (N) were fixed to crystallographic values; R (interatomic distance), σ^2 (Debye-Waller-type factor based on a Gaussian distribution of interatomic distances), and ΔE_0 (the difference between the threshold Fermi level of the theoretical phase shift and backscattering amplitude functions and the experimental data) were given initial seed values and they were allowed to move during the non-linear least squares fitting routine.

3. Results and discussion

AS on the sets of samples CIEMAT-Unat are presented in Fig. 3. The almost systematic worsening of resolution, expressed as FWHM (full width at half maximum), with the increasing of the electrodeposition time is observed by the FWHM graphic in the insert. Also it is well perceived by the U-234 doublet behavior, where the "shoulder" disappears when electrodeposition time increases. This result suggests as a general trend the resolution worsening with electrodeposition time observed in Ref. 13.

3.1. X-ray scattering from grazing incidence on uranium sources

GI-XRD on sources set CIMAV-UAc was performed with different incidence angles, from $\phi = 0.0$ to $0.8°$. Fig. 4 shows

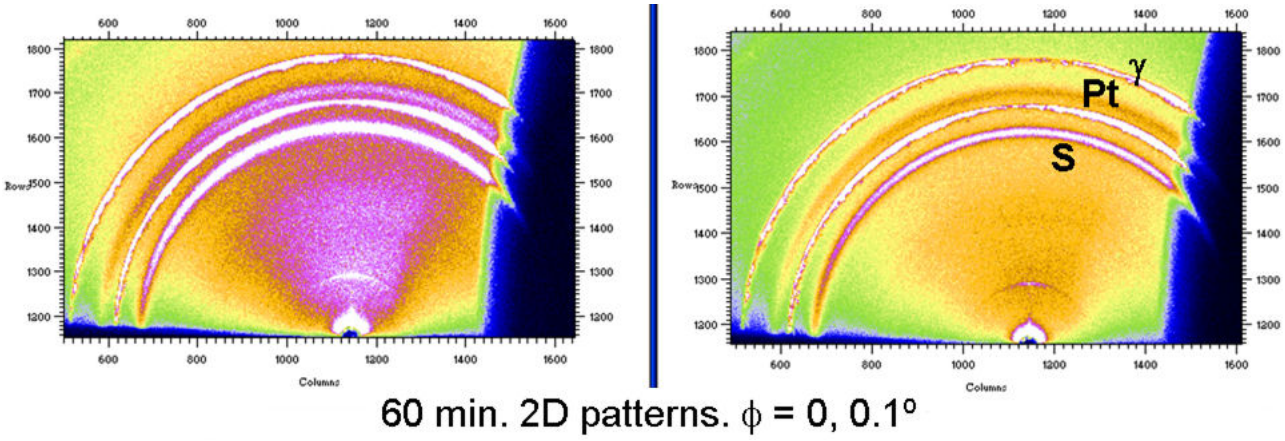

FIGURE 4. 2-D XRD patterns of sample CIMAV-UAc-60. Characteristic Debye rings from steel substrate (γ), as well as electrodeposited Pt and schoepite (S) are identified.

one of the measured 2-D patterns for the sample UAc-60. The 2-D patterns were integrated by azimuthal angle, and 1-D patterns were obtained.

Working on 1-D patterns, different compounds were identified and some other determinations were performed. Phase identification was carried out by means of the ICSD data base [23]. Particularly, for the elucidation of the uranium compound, present in the analyzed sources, several options were considered. Some evidence of broad peaks in the low 2θ zone at many patterns may be attributed to uranium compounds of large reticular parameters. The best candidate for the uranium phase was uranium oxyhydroxide known as schoepite. Figure 5 shows the computer-modeled diagram obtained for this purpose, performed on a 1-D pattern of the source UAc-60. Analyzing the profile of (broad) peaks in the case of the Pt and schoepite phases and applying the Scherrer equation [24], crystallite dimensions of these phases were estimated. Pt peaks lead to crystallite sizes $t \sim 20$ nm and ~ 5 nm. Schoepite diffraction signals indicate poorly crystallized grains ($t < 5$ nm). The broad Pt peaks are located either on the left, below or on the right of the sharp Pt peaks, depending on the location of the nanocrystals on the deposited source. The peaks, attributed to schoepite in the 60 min 1-D pattern, may have different locations in the other patterns. This way, the schoepite identification is not univocal by GI-XRD results.

Split-broadened peaks in Fig. 5 are produced by bi-modal size distribution of Pt grains. Dispersion in the location of the broadened Pt peaks is produced by heterogeneity in the distribution of Pt nano particles on the source surface. This feature was observed and confirmed in all the three to six GI-XRD patterns recorded of each CIMAV Ac sources.

Grazing incidence X-ray scattering results suggest that:

1) Bi-modal presence of Pt in deposits is explained as follows. There is a well crystallized Pt layer, consequence of some *old* Pt deposit and registered in GI-XRD patterns as sharp peaks. Also, there is a *new* nanocrystalized Pt that appears on apparently isolated places on the surface of the deposit. That's why the broad Pt peaks in GI-XRD patterns locate from left to right around the Pt sharp peaks. These *new* Pt tends to grow or even may have coalescence when become *aged* Pt. This phenomenon has been attributed [25] to the isolated location of nanosized clusters on the sample, resulting in the dispersion of the sample-detector distance.

2) Deposited uranium forms poorly crystallized layers probably of schoepite, with crystal size of approximately 5 nm and layer thickness of 50 nm on average (this figure is given by the amount of electrodeposited uranium and the deposit area).

3.2. XANES study of oxidation state of samples

Figure 6 shows the comparison of the XANES spectra from CIMAV-UAc sources with uraninite-UO_2 (with U^{+4}) and becquerelite (uranyl mineral with U^{+6}) spectra, measured in

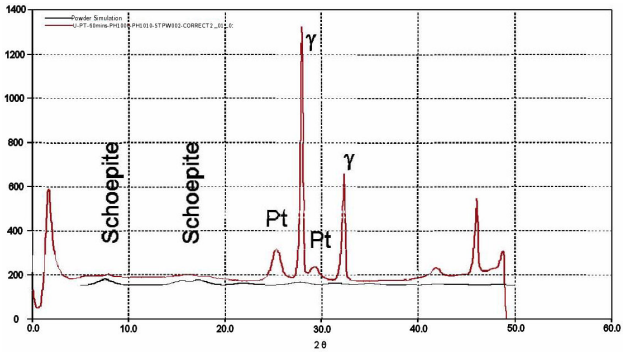

FIGURE 5. 1-D diffraction pattern obtained by azimuthal integration of a representative 2-D pattern from the source UAc-60. For this sample, patterns collected with different incidence angles were practically coincident. Peaks produced by characteristic phases are identified. The weak pattern in the lower part is a computer-modeled diagram corresponding to nanocrystalline schoepite.

TABLE II. EXAFS fitting results and schoepite XRD derived interatomic distances for the CIEMAT Unat sources.

			EXAFS				XRD	
sample	Shell		N^+	R(Å)	$\square^{\square}\ \sigma^2$(Å^2)	$\square\ \Delta E_o$	R %	R(Å)
20 minutes	O_{ax}		2			15.7(1.3)	3.9	
		O_1	1	1.800(7)	0.0032(5)			1.74(2)
		O_2	1	1.855(7)	0.0032(5)			1.79(2)
	O_{eq}							
		O_{17}	1	2.29(1)	0.0043(26)			2.29(2)
		OH_1	1	2.40(1)	0.0043(26)			2.40(2)
		OH_2	1	2.42(1)	0.0043(26)			2.42(2)
		OH_3	1	2.53(1)	0.0043(26)			2.53(2)
		OH_4	1	2.63(1)	0.0043(26)			2.63(2)
	U							
	U_{5-1}		1	3.81(4)	0.012(6)			3.83(2)
	U_7		1	3.85(4)	0.012(6)			3.87(2)
	U_6		1	4.04(4)	0.012(6)			3.99(2)
	U_{5-2}		1	4.04(4)	0.012(6)			4.09(2)
	U_2		1	4.30(12)	0.012(6)			4.45(2)
			EXAFS				XRD	
sample	Shell		N^+	R(Å)	$\square^{\square}\ \sigma^2$(Å^2)	$\square\ \Delta E_o$	R %	R(Å)
40 minutes	O_{ax}		2			15.6(1.3)	5.3	
		O_1	1	1.799(7)	0.0035(5)			1.74(2)
		O_2	1	1.853(7)	0.0035(5)			1.79(2)
	O_{eq}							
		O_{17}	1	2.29(2)	0.005(3)			2.29(2)
		OH_1	1	2.40(2)	0.005(3)			2.40(2)
		OH_2	1	2.42(2)	0.005(3)			2.42(2)
		OH_3	1	2.53(2)	0.005(3)			2.53(2)
		OH_4	1	2.63(2)	0.005(3)			2.63(2)
	U							
	U_{5-1}		1	3.74(2)	0.006(2)			3.83(2)
	U_7		1	3.77(2)	0.006(2)			3.87(2)
	U_6		1	3.92(3)	0.006(2)			3.99(2)
	U_{5-2}		1	4.02(3)	0.006(2)			4.09(2)
	U_2		1	4.21(4)	0.006(2)			4.45(2)
			EXAFS				XRD	
sample	Shell		N^+	R(Å)	$\square^{\square}\ \sigma^2$(Å^2)	$\square\ \Delta E_o$	R %	R(Å)
60 minutes	O_{ax}		2			14.6(2.2)	6.5	
		O_1	1	1.79(1)	0.0035(6)			1.74(2)
		O_2	1	1.85(1)	0.0035(6)			1.79(2)
	O_{eq}							
		O_{17}	1	2.41(17)	0.015(6)			2.29(2)
		OH_1	1	2.33(17)	0.015(6)			2.40(2)
		OH_2	1	2.35(17)	0.015(6)			2.42(2)
		OH_3	1	2.46(17)	0.015(6)			2.53(2)
		OH_4	1	2.51(17)	0.015(6)			2.63(2)
	U							
	U_{5-1}		1	3.96(3)	0.007(2)			3.83(2)
	U_7		1	3.99(3)	0.007(2)			3.87(2)
	U_6		1	3.73(4)	0.007(2)			3.99(2)
	U_{5-2}		1	3.83(4)	0.007(2)			4.09(2)
	U_2		1	4.19(4)	0.007(2)			4.45(2)

( )Estimated standard deviations;

+ Fixed to crystallographic values during fitting

similar conditions as reference compounds at SSRL. Feature A is the maximum at resonance ("white line"), which is broader in uranyl compounds; feature B is characteristic of uranyl species and feature C accounts for the backscattering of the photoelectron by the second sphere neighbors [26].

We may observe that all CIMAV-UAc sources show the white line broad peak characteristic of the uranyl ion structure. Nevertheless, its energy and feature B are enhanced in the source prepared during 20 minutes. As it was discussed in Ref. 13, concerning the uranium oxidation states, based on the literature [27-31], different uranium oxidation states produce UL_3 edge shifts towards higher energies in the order UO_2, U_3O_8, UO_3 due to reduced shielding of the core electrons associated with the increase in mean valence state across the oxidation series. Figure 6 shows the position of the absorption edge in the XANES spectra. The insert indicates the relative position of the white line of uranium species in the sources in relation to the extreme oxidation states +4 and +6. Based on reported values cited above and on the measured reference compounds, UAc-60 corresponds to a mixture of U(IV) and U(V), while UAc-20 and UAc-40 correspond to a mixture of U(V) and U(VI), with UAc-20 closer to U(VI). All these features are in agreement with the results presented in Ref. 13.

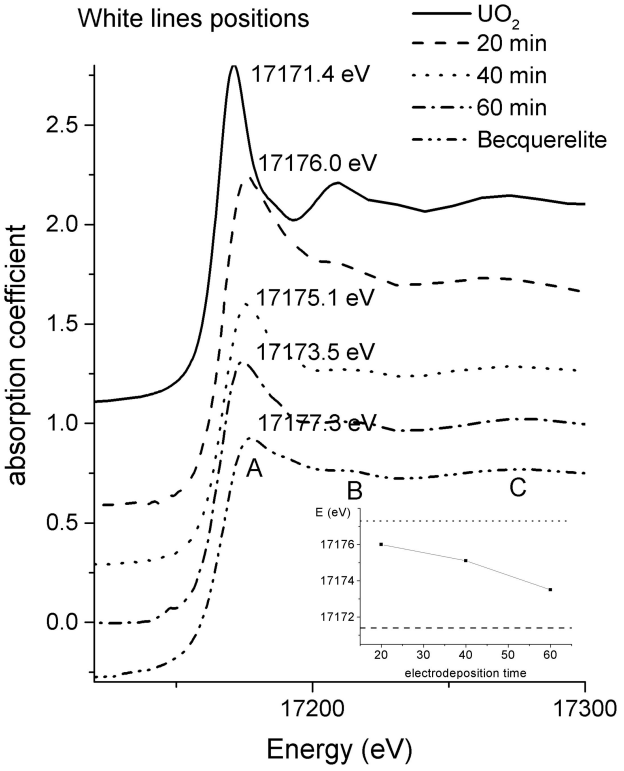

FIGURE 6. XANES spectra of the UL_3-edge of CIMAV-UAc sources and reference compounds: UO_2 (uraninite) and becquerelite synthetic mineral. The insert shows the energy positions of white lines for CIMAV-UAc sources, given by the electrodeposition time in minutes, relative to U(IV) white line position (dashed at bottom) and to U(VI) position (top dots).

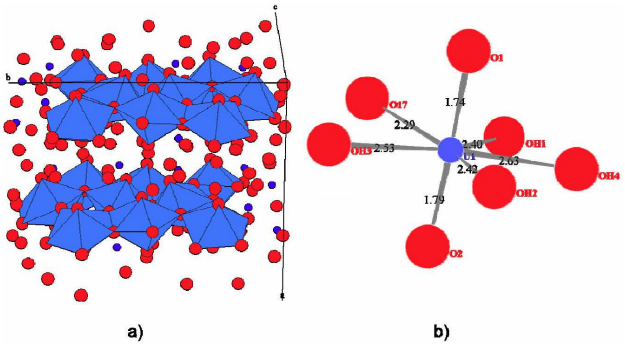

FIGURE 7. a) Unit cell of schoepite, showing uranium atoms in blue and oxygen in red. Two layers formed by pentagonal bipyramids more or less parallel to b-c planes are presented. b) Details of the uranyl O_{ax} and O_{eq} distances for the considered representative bipyramid.

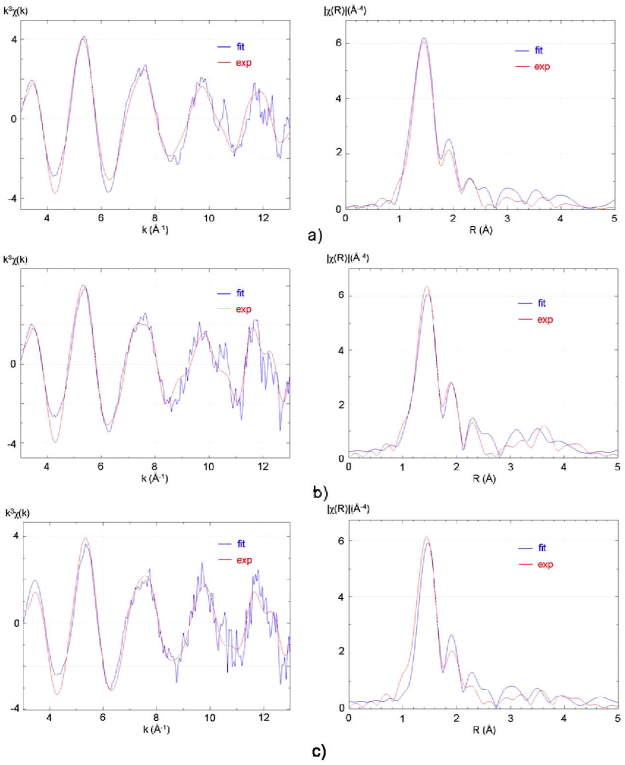

FIGURE 8. Spectra of CIEMAT Unat sources: EXAFS function fitting in χ (left) and fitting in R (right). There are shown the spectra corresponding to a) 20 minutes, b) 40 minutes and c) 60 minutes.

3.3. EXAFS modeling

After subtraction of background for obtaining EXAFS function, EXAFS spectra are similar to that of oxyhydroxides reported by Catalano and Brown [32]. Taking into account the results of the preceding section, as well as the Hansen theory for electrodeposition of actinides and other compounds [33], schoepite oxyhydroxide and uranyl hydroxide structures were modeled. In the paper of Beesley *et al.* [13],

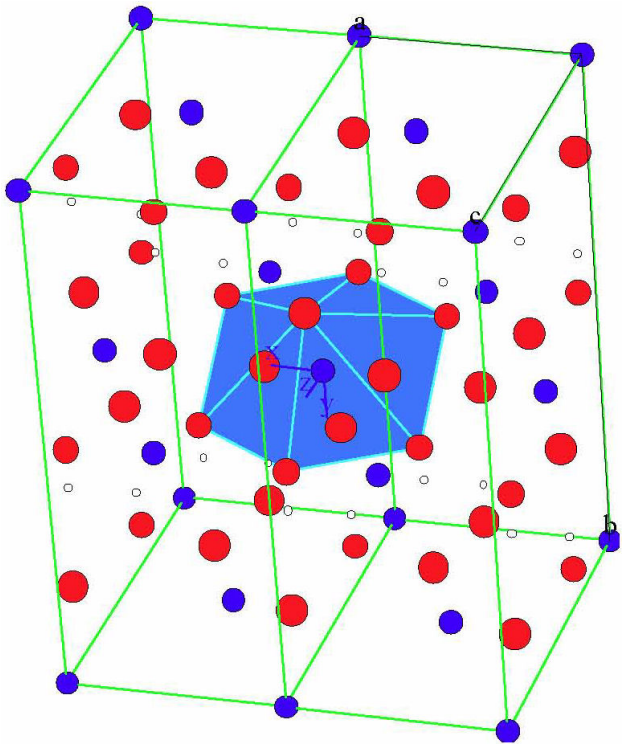

FIGURE 9. Unit cell of uranyl hydroxide, showing uranium atoms in blue and oxygen in red. Two unit cells are shown, in order to present the almost regular hexagonal based bipyramid, formed in the b-c face.

EXAFS experiment was used for determining the coordination number of equatorial oxygens O_{eq} located in the bipyramids formed together with the uranyl axial oxygens O_{ax}. In the present representation, the structure of uranyl hydroxide has five O_{eq}, while schoepite has six ones. In addition, now is presented an attempt of fitting the uranium coordination sphere inside the cluster of radius R=4.5 Å. The results of both fittings will be compared for giving conclusions.

EXAFS interpretation by fitting of ab initio functions of schoepite (structural data obtained from [21]) is complicated by the range of first- and second-shell interatomic distances. Figure 7 shows the structure of the unit cell, together with the "star" formed by uranium atom with the oxygens forming the pentagonal bipyramids. There are many equivalent position of uranium in bipyramids inside the unit cell, and the distinct scattering paths are too numerous to be fit independently. Similar paths have to be grouped or, instead, assume that one set of path is representative of the others. The last one was the way selected in this work. Furthermore, there is one site in the equatorial plane of the bipyramid occupied by an O^{2-} anion, while there are four sites corresponding to hydroxyls, with different distances. For fitting, the presence of no hydrogen was considered and σ^2; the so-called Debye-Waller factors, were considered the same for each close interatomic distance: U_{abs}- O_{ax}, U_{abs}- O_{eq} and five U_{abs}-U_{scatt} atoms inside the cluster of radius R=4.5 Å. Moreover, ΔE_0 value was fitted at the beginning of the procedure, then was considered the same for all shells and fixed. Only the first MS path was included in the fit for both uranium species. The R factor value was used to evaluate the quality of the fits. Table II presents the results for the three different electrodeposition times. Figure 8 shows the corresponding graphics for EXAFS functions and Fourier Transforms (FT).

Uranyl axial bond distances agree with the XRD-derived reference within the uncertainties in all averaged by electrodeposition time fitting of spectra. That is not the general case for the other distances. The relatively high values of ΔE_0 may be considered as not so large, if taking into account that the U LIII absorption edge is located at 17172.25 eV. Referring to discussion in the paper of Catalano and Brown [32], schoepite distinct shells with differences in interatomic distances close to the intrinsic distance resolution ΔR of EXAFS spectroscopy ($\Delta R=\pi/(2\Delta k\ \text{Å}^{-1})=\pi/(7\ \text{Å}^{-1})$=0.22 Å, where Δk is the k-range of data being fitted) were not accurately fit, causing significant errors in interatomic distances and Debye-Waller factors (see Table II). However the accuracy of the fits for short times, assessed by the χ^2_ν value, is good, as it can also be seen graphically in Fig. 8.

Figure 9 presents the unit cell of the uranyl hydroxide. Results for uranyl hydroxide ab initio fitting of the 3 different EXAFS spectra are shown in Table III. The hydroxide structure is very regular (see interatomic distances from XRD in Table III), in contrast to the schoepite structure (Table II). To show one hexagonal bipyramid in uranyl hydroxide, two contiguous unit cells are shown. Nevertheless, the quality of the fitting is worse, if taking into account the accuracy of parameters for the equatorial oxygen and uranium shells.

As a result of comparing Table II and III, several conclusions may be given: 1) the uranyl axial oxygens are probably in position closer to the one of uranyl hydroxide, because the fitting of schoepite produces U_{abs}-O_{ax} distances greater than those from XRD. 2) Equatorial oxygens probably have coordination number equal to 5, because the schoepite fitting shows results with better accuracy than those from the uranyl hydroxide fitting. Moreover, the results of Table III show interatomic distances much lower than those from XRD. Probably the bipyramids are irregular. 3) Inter-uranium distances U_{abs}-U_{scat} are lower than those from XRD in both fittings. It could be a result of lack of information in χ(k), or a result of low crystalinity of uranyl compounds. 4) There is a general trend in the two tables showing a worsening of fittings when increasing electrodeposition time. This phenomenon goes along with the changes observed in XANES spectra, which for longer times have shown a shift of the absorption edge position (or the white line's) to those proper of uranium reduced species.

4. Conclusions

Synchrotron radiation studies on electrodeposited uranium sources have provided valuable information about the Pt and U compounds produced by the Hallstadius method of electrodeposition.

TABLE III. EXAFS fitting results and uranyl hydroxide XRD derived interatomic distances for the CIEMAT Unat sources.

				EXAFS				XRD
sample	Shell		N^+	R(Å)	σ^2(Å^2)	ΔE_o	R%	R(Å)
merge 20	O_{ax}		2				2.1	
		O_1	2	1.801(5)	0.004(8)*	7.89(1.5)		1.79(2)
	O_{eq}		6					
		O_{2-1}	4	2.387(8)	0.019(1)*	11.664(32)		2.49(2)
		O_{2-2}	2	2.393(8)	0.019(1)*	11.664(32)		2.50(2)
	U		1					
			1	3.598(4)	0.003*	14.418*		4.03(2)

				EXAFS				XRD
sample	Shell		N^+	R(Å)	σ^2(Å^2)	ΔE_o	R%	R(Å)
merge 40	O_{ax}		2				2	
		O_1	2	1.812(5)	0.0040(7)*	10.198(1.5)		1.79(2)
	O_{eq}		6					
		O_{2-1}	4	2.339(8)	0.018(1)*	9.111(32)		2.49(2)
		O_{2-2}	2	2.345(8)	0.018(1)*	9.111(32)		2.50(2)
	U		1					
			1	3.62(4)	0.003*	7.217*		4.03(2)

				EXAFS				XRD
sample	Shell		N^+	R(Å)	σ^2(Å^2)	ΔE_o	R%	R(Å)
merge 60	O_{ax}		2				2.6	
		O_1	2	1.814(11)	0.0047(9)*	10.15(1.81)		1.79(2)
	O_{eq}		6					
		O_{2-1}	4	2.308(11)	0.019(2)*	7.67(1.33)		2.49(2)
		O_{2-2}	2	2.314(11)	0.019(2)*	7.67(1.33)		2.50(2)
	U		1					
			1	3.628(109)	0.01*	7.903*		4.03(2)

( ) Estimeted standard deviations.

+ Fixed to crystallographics values during fitting.

*Parameter fixed during fitting after a previous aproximation.

The GI-XRD results inform that metallic platinum is detected simultaneously well and poorly crystallized. The location of the broad peaks associated to the nanometric *new* platinum appears in several patterns at different sides of the sharp Pt peaks (from *old* well crystallized Pt). Deposited uranium forms poorly crystallized layers probably of schoepite, with crystal size of approximately 5 nm.

XANES shifts of the white lines energy suggest that the electrodeposition carried out for short periods (20 minutes) produce more oxidized precipitates than those undertaken for longer times. This result is coincident with that obtained in Ref. 13, and it is not trivial, since one of the differences between the XAFS experiment discussed in Ref. 13 and the one presented here is that in the later, the sources were prepared very shortly before the XANES study. Another point of interest is that in both cases the sources were kept in an aerobic environment at all times. Surprisingly, reduced species of uranium present in UAc-60 were not oxidized in air. All these features are in agreement with the results presented in Ref. 13.

EXAFS results provide a confirmation of the oxyhydroxide character of the uranium species on the sources. Probably it is a mixture of schoepite, uranyl hydroxide and uraninite (a very regular structure of UO_2), which represents the U(IV) form of uranium compounds. The mixture composition would develop as electrodeposition progresses. The observed trend of worsening the fitting quality when electrodeposition time increases is congruent with the XANES result about the presence of more reduced species of uranium at the source surface.

Detection of uranyl oxyhydroxides is consistent with the Hansen theory and confirms the conclusion given in Ref. 13

about predominance of uranyl-type structures with pentagonal bipyramids.

5. Acknowledgements

We want to thank John Bargar, Carol Morris and Sam Webb from SSRL for their help at laboratory and beam line. John Bargar has given the uraninite XANES spectrum as model compound. This study has been partially supported by SEP-CONACYT Project 26040. Portions of this research were carried out at the Stanford Synchrotron Radiation Lightsource, a national user facility operated by Stanford University on behalf of the U.S. Department of Energy, Office of Basic Energy Sciences. The SSRL Structural Molecular Biology Program is supported by the Department of Energy, Office of Biological and Environmental Research, and by the National Institutes of Health, National Center for Research Resources, Biomedical Technology Program.

1. S. Pomme *et al., Metro* **46** (2009) 439.
2. C. Roselli, D. Desideri, and M. Assunta Meli, *Microchem. J.* **91** (2009) 181.
3. H. Michel, D. Levent, V. Barci, G. Barci-Funel, and C. Hurel, *Talanta* **74** (2008) 1527.
4. M. Minteer *et al., Health Phys.* **92** (2007) 488.
5. H. Sugiyama *et al., J. Toxicol. Sci.* **34** (2009) 417.
6. A. Martín Sánchez, M. Jurado Vargas, M.J. Nuevo Sánchez, and A. Fernández Timón, *Appl. Radiat. Isot.* **66** (2008) 804.
7. F. Vera Tomé, M. Jurado Vargas, and A. Martin Sánchez, *NIMPA* **348** (1994) 183.
8. E. Garcia-Torano, *Appl. Radiat. Isot.* **64** (2006) 1273.
9. N.A. Talvitie, *Anal. Chem.* **44** (1972) 280.
10. J.L. Ferrero Calabuig *et al., NIM A* **369** (1996) 603.
11. J. L. Ferrero Calabuig *et al., NIM B* **136** (1998) 290.
12. R. Weber, P. Vater, R.A. Esterlund, and P. Patzelt, *NIM A* **423** (1999) 468.
13. A.M. Beesley *et al., Appl. Radiat. Isot.* **67** (2009) 1559.
14. L. Hallstadius, *NIM Phys Res* **223** (1984) 266.
15. R.F. Mitchell, *Anal. Chem.* **32** (1960) 326.
16. L. Fuentes-Montero *et al., Integrated Ferroelectrics* **101** (2008) 101.
17. N. Stojanovic, "Experimental Station 11-3, SSRL. " (2009) http://www-ssrl.slac.stanford.edu/beamlines/bl11-3/.
18. A.P. Hammersley, in *ESRF International Report No. ESRF98HA01T. Program available at* (2004). http://www.esrf.eu/computing/scientific/FIT2D
19. B. Ravel and M. Newville, *J. Synch. Rad.* **12** (2005) 537.
20. M. Newville, *J. Synch. Rad.* **8** (2001) 322.
21. R.J. Finch, M.A. Cooper, F.C. Hawthorne, and R.C. Ewing, *Can Mineral* **34** (1996) 1071.
22. J.C. Taylor and H.J. Hurst, *Acta Crys. B* **27** (1971) 2018.
23. R. Allmann, R. Hinek, G. Bergerhoff, and I.D. Brown, *FIZ Karlsruhe* (National Institute of Standards and Technology (NIST), 2009).
24. D.M. Smilgies, *J. Appl. Crystallogr.* **42** (2009) 1030.
25. M. Torres Sancho, in PhD Thesis, *Instituto de Química y Materiales Alvaro Alonso Barba*, (Universidad Carlos III de Madrid, Leganés, Madrid, 2009) p. 172.
26. C. Den Auwer *et al., New J. Chem.* **27** (2003) 648.
27. M.C. Duff, C. Amrhein, P.M. Bertsch, and D.B. Hunter, *Geochim. Cosmochim. Acta* **61** (1997) 73.
28. J. Jernstrom *et al., J. Anal. At. Spectrom.* **19** (2004) 1428.
29. B. Salbu *et al., J. Environ. Radioact.* **78** (2005) 125.
30. M.A. Denecke, *Coord. Chem. Rev.* **250** (2006) 730.
31. A.V. Soldatov *et al., J. Solid State Chem.* **180** (2007) 54.
32. J.G. Catalano and G.E. Brown Jr, *Am. Mineral.* **89** (2004) 1004.
33. P.G. Hansen, *J. Inorg. Nucl. Chem.* **12** (1959) 30.